AGU PUBLICATIONS

JGR

Journal of Geophysical Research: Atmospheres

RESEARCH ARTICLE
10.1002/2014JD021909

Key Points:
- $O(^3P) + O_2$ isotope exchange rapidly equilibrates the isotopic distribution in O_2
- $O(^3P) + O_2$ governs isotopic bond ordering in atmospheric O_2
- Tropospheric $^{18}O^{18}O$ and $^{17}O^{18}O$ trace oxygen photochemistry near the surface

Supporting Information:
- Readme
- Table S1

Correspondence to:
L. Y. Yeung,
lyyeung@ucla.edu

Citation:
Yeung, L. Y., J. L. Ash, and E. D. Young (2014), Rapid photochemical equilibration of isotope bond ordering in O_2, *J. Geophys. Res. Atmos.*, *119*, 10,552–10,566, doi:10.1002/2014JD021909.

Received 15 APR 2014
Accepted 15 AUG 2014
Accepted article online 19 AUG 2014
Published online 10 SEP 2014

Rapid photochemical equilibration of isotope bond ordering in O_2

Laurence Y. Yeung[1], Jeanine L. Ash[1], and Edward D. Young[1]

[1]Department of Earth, Planetary, and Space Sciences, University of California, Los Angeles, California, USA

Abstract The abundances of $^{18}O^{18}O$ and $^{17}O^{18}O$ in the atmosphere were recently found to be enriched relative to the stochastic distribution of isotopes in O_2. The enrichment is believed to arise from $O(^3P) + O_2$ isotope exchange reactions, which reorder the isotopes in O_2 to a distribution that favors bonds between heavy isotopes. Theoretical predictions and laboratory experiments suggest that the reordered distribution of isotopes should reflect internal isotopic equilibrium, but a laboratory test of this hypothesis for the complete O_2 isotopologue system has not yet been realized. Here we use a simple photochemical experiment that reorders the isotopes in O_2 at temperatures between 200 K and 350 K. Using simultaneous measurements of five O_2 isotopologues, we show that $O(^3P) + O_2$ reorders the isotopes in O_2 to isotopic equilibrium. Furthermore, we use this scheme to calibrate measurements of isotopic ordering in samples of O_2, obtaining Δ_{36} and Δ_{35} values within ±0.1‰. Measurements of atmospheric O_2 sampled at the University of California, Los Angeles, from 2012 to 2014 have mean values of $\Delta_{36} = 1.97 \pm 0.07$‰ and $\Delta_{35} = 1.0 \pm 0.1$‰ (2 SE; $n = 23$), with no detectable long-term trend. These measurements are consistent with values for air reported earlier, but with a threefold to fourfold improvement in precision. Together, the experiments and observations support the case that isotopic ordering in tropospheric O_2 is altered by $O(^3P) + O_2$; however, they also suggest that tropospheric Δ_{36} and Δ_{35} values do not reflect complete isotopic equilibration in the troposphere. Isotopic ordering in atmospheric O_2 likely reflects the decadal-scale balance of stratospheric and tropospheric air masses modulated by variations in tropospheric photochemistry and convection.

1. Introduction

Molecular oxygen is the most important biogeochemical gas in the atmosphere. It holds a unique record of biological, hydrological, and photochemical signatures within its isotopic composition. This record provides constraints on the coevolution of the biosphere, hydrosphere, and atmosphere on time scales relevant to both abrupt and protracted climate change [*Bender et al.*, 1994; *Luz et al.*, 1999; *Blunier et al.*, 2002; *Landais et al.*, 2007; *Severinghaus et al.*, 2009]. Until recently, however, only the bulk isotopic composition of O_2 (i.e., its $^{18}O/^{16}O$ and $^{17}O/^{16}O$ ratios) had been studied. In nature, this composition varies primarily in response to biological oxygen cycling, although the influence of stratospheric photochemistry can also be detected [*Guy et al.*, 1989, 1993; *Luz et al.*, 1999; *Angert et al.*, 2003; *Young et al.*, 2014].

The recent addition of $^{18}O^{18}O$ and $^{17}O^{18}O$ to isotopic analyses of O_2 revealed new information recorded in atmospheric O_2 [*Yeung et al.*, 2012]. The simultaneous measurements of five O_2 isotopologues ($^{16}O^{16}O$, $^{16}O^{17}O$, $^{16}O^{18}O$, $^{17}O^{18}O$, and $^{18}O^{18}O$) showed that a signature of ^{16}O, ^{17}O, and ^{18}O ordering in O_2 was also present and controlled largely by the photochemistry of the odd oxygen system (i.e., $O_3 + O$). This isotopic ordering in atmospheric O_2 was found to be nonstochastic, with $^{18}O^{18}O$ and $^{17}O^{18}O$ enriched relative to a random distribution of isotopes (i.e., $\Delta_{36} > 0$ and $\Delta_{35} > 0$, respectively). To explain this observation, *Yeung et al.* [2012] hypothesized that $O(^3P) + O_2$ isotope exchange reactions reorder the isotopes in O_2 toward an isotopic equilibrium that depends on temperature: At low temperatures, the $^{18}O^{18}O$ and $^{17}O^{18}O$ enrichments should be relatively high, whereas at higher temperatures, the enrichments are expected to be low. Moreover, because temperatures are not uniform in the atmosphere, the dynamic balance between tropospheric and stratospheric processes was expected to have a strong influence on atmospheric Δ_{36} and Δ_{35} values. However, a definitive confirmation of the kinetics of isotopic reordering and its effects on Δ_{36} and Δ_{35} values at different temperatures was lacking.

In this study, we use photochemical experiments to show that isotope exchange reactions between $O(^3P)$ (i.e., oxygen atoms in their ground electronic state) and O_2 can explain both the kinetics of isotopic ordering and

the steady state Δ_{36} and Δ_{35} values in O_2 upon irradiation with UV light. We investigated the time evolution of Δ_{36} and Δ_{35} values at 300 K and compared the results to predictions from theoretical calculations [*Kaye and Strobel*, 1983; *Hathorn and Marcus*, 2000; *Fleurat-Lessard et al.*, 2003]. We also compared Δ_{36} and Δ_{35} values at steady state to the values predicted at isotope exchange equilibrium [*Wang et al.*, 2004]. Finally, we used these experiments to calibrate and interpret 14 months of Δ_{36} and Δ_{35} measurements in air at the University of California, Los Angeles (UCLA). These results constitute a high-precision calibration method for Δ_{36} and Δ_{35} values (±0.1‰) that can be replicated independently in other laboratories for a wide variety of chemical and biogeochemical applications. They also validate the longstanding hypothesis that O_2 quickly reaches internal isotopic equilibrium in the ozone photochemical system [*Kaye and Strobel*, 1983; *Anderson et al.*, 1997; *Hathorn and Marcus*, 2000; *Fleurat-Lessard et al.*, 2003].

2. Isotopic Ordering: Definitions

Quantities of $^{18}O^{18}O$ and $^{17}O^{18}O$ (i.e., mass-36 and mass-35 O_2) are reported relative to the stochastic distribution of isotopes in O_2. Using the notation described in *Yeung et al.* [2012], where ^{m}R indicates molecular ratios, we characterize proportional $^{18}O^{18}O$ abundances using

$$\Delta_{36} = \left(\frac{^{36}R_{\text{measured}}}{^{36}R_{\text{stochastic}}} - 1\right), \tag{1}$$

where

$$^{36}R_{\text{measured}} = \frac{[^{36}O_2]}{[^{32}O_2]} \quad \text{and} \quad ^{36}R_{\text{stochastic}} = \frac{[^{18}O][^{18}O]}{[^{16}O][^{16}O]} = \left(^{18}R\right)^2. \tag{2}$$

Similar Δ_n terminology describes proportional abundances of $^{17}O^{18}O$; however, an additional factor of 2 is present in the stochastic distribution, i.e.,

$$^{35}R_{\text{measured}} = \frac{[^{35}O_2]}{[^{32}O_2]} \quad \text{and} \quad ^{35}R_{\text{stochastic}} = \frac{2[^{17}O][^{18}O]}{[^{16}O][^{16}O]} = 2\times{}^{17}R^{18}R, \tag{3}$$

because $^{17}O^{18}O$ has two symmetrically equivalent isotopomers. Enrichments and deficits in Δ_n notation are reported in per mil (‰): Δ_{36} and Δ_{35} values equal to zero represent a random distribution of isotopes, whereas a positive or negative Δ_n value represents an overabundance or under-abundance of $^{18}O^{18}O$ or $^{17}O^{18}O$, respectively, relative to the stochastic distribution defined in equations (2) and (3). These values represent isotopic ordering when they change as a result of bond alteration, such as during isotope exchange reactions.

We note that equilibrium in the context of isotopic ordering references an equilibrium distribution of isotopes among molecules comprising a single molecular species. Isotopic equilibrium between multiple species (e.g., between O_2 and O_3) depends on the partitioning of isotopes among all relevant isotopologues, which can be significantly more complex. In this paper, we investigate only isotopic ordering in O_2, which can be established independently from, and on different time scales than, the bulk isotopic partitioning that occurs between the oxygen-containing molecular species in a gas-phase photochemical system. The reader is directed to the literature on the isotope effects of O_3 formation for discussions of photochemical equilibrium between O_2 and O_3 [*Janssen*, 2005].

3. Laboratory Experiments

3.1. Experimental Apparatus

Photochemical experiments were carried out in a 1000 mL round-bottom Pyrex flask (radius = 6.2 cm; see Figure 1). It had a single vacuum valve attached via 13 cm × 9 mm ID tube and a quartz-and-Pyrex transition tube inset (9 cm × 11 mm ID, 13 mm OD inside the bulb). The length of the quartz tubing inside the bulb was 7.6 cm; a 12 cm glass extension to the exterior was sealed against the quartz-to-Pyrex transition and to the bulb. Ultraviolet light was generated with a Pen-Ray mercury line source (UVP model 3SC-9) inserted through the open extension to illuminate the bulb through the short length of quartz (7.6 cm) inside. A flow of nitrogen was utilized to flush out potential UV absorbers between the lamp and the quartz. To vary the reaction temperature, the entire apparatus was submerged in a large dewar filled with either water or liquid N_2-cooled ethanol at different temperatures.

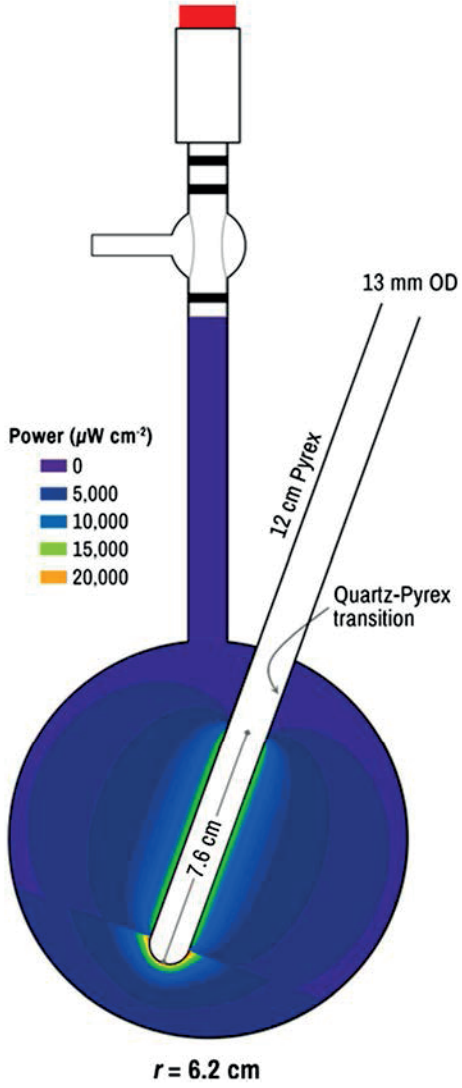

Figure 1. Schematic diagram of the photolysis bulb. A contour diagram of the calculated irradiance is depicted in the bulb's interior.

Thermocouples (Type K) were used to monitor the temperature of the liquid bath and the quartz finger. Bath temperatures were maintained to within ±2°C.

This geometrically and optically simple apparatus allows one to calculate the reaction conditions. For example, the photon flux into the bulb can be calculated based on the manufacturer-specified irradiances at 254 nm (5400 μW cm^{-2} at 1.9 cm) and 185 nm (3% of flux at 254 nm), the optical transmission through the quartz (80% at 254 nm, 30% at 185 nm), and the geometry of the quartz portion of the tube. The typical photon flux at the surface of the quartz finger was 6×10^{16} cm^{-2} s^{-1}, and the volume-weighed mean number density in the bulb is calculated to have been 2.3×10^{15} photons cm^{-3} s^{-1} (see section 3.2.1).

Elevated temperatures were observed inside the finger during lamp operation, necessitating a calculated adjustment to gas temperatures above the bath temperature. The fixed surface area of the finger (39 cm^2) and bulb (487 cm^2) allowed us to calculate the mean internal temperature based on the Stefan-Boltzmann law. For example, when the bulb was immersed in water at 298 K, the temperature of the finger was typically 343 K at steady state after the lamp had warmed up. We calculated a mean gas temperature of $T_{gas} = 302$ K using the relationship $T_{gas}^4 = (39/526) \times T_{finger}^4 + (487/526) \times T_{bath}^4$. This temperature, which was 4 K higher than the immersion bath temperature, was used to calculate the equilibrium temperature for isotopic ordering inside the bulb.

Samples of O_2 were analyzed immediately following photolysis because both thermal and photolytic decomposition of O_3 can reorder the isotopes in the O_2 sample. Indeed, an O_2 sample that was initially equilibrated photochemically at 278 K was reordered to room temperature isotopic equilibrium after being stored for several months in room light and at room temperature (see section 3.4). Glass and quartz have very low reactivity, however, so the presence of O_3 likely catalyzed the isotopic reordering in this instance. Long-term storage in glass and quartz vessels may not necessarily equilibrate the distribution of isotopes in O_2 without such a catalyst.

3.2. Photochemical Model

3.2.1. Mercury Lamp Irradiance

The 254 nm and 185 nm photon fluxes derived in the previous section were converted to mean photon number density for input into a photochemical model. The simple geometry of the apparatus enabled this calculation: The quartz portion of the interior finger was treated as a cylinder (7 cm × 13 mm diameter) plus a hemispherical end ($r = 6.5$ mm). The photon flux entering the evacuated part of the bulb through the quartz finger was then calculated using the view factor method [*Modest*, 2013]:

$$\text{Power} = \frac{E_{UV}}{2\pi r l_{tot}} F_{total}, \tag{4}$$

where E_{UV} is the power output of the lamp in microwatts, r is the lamp's radius (4.75 mm), l_{tot} is the total length of the cylinder (7 cm; the hemispheric end was treated separately), and F_{total} is the fraction of the

lamp's power output incident on a given area dA in free space (i.e., its view factor). This view factor was computed by splitting it into two sections for any given position in between the two ends of the lamp,

$$F_{\text{total}} = F_{l_1} + F_{l_2}, \tag{5}$$

where l_1 and l_2 represent the distances from the ends of the lamp for any point in space projected onto the cylindrical lamp. The view factor for each of these segments is computed as a function of l and d (the distance from the lamp) according to the following equation:

$$F_l = \frac{L}{\pi H}\left[\frac{1}{L}\tan^{-1}\left(\frac{L}{\sqrt{H^2-1}}\right) - \tan^{-1}(M) + \frac{X-2H}{\sqrt{XY}}\tan^{-1}\left(M\sqrt{\frac{X}{Y}}\right)\right], \tag{6}$$

where L, H, X, Y, and M are defined as follows:

$$L = l/r, \tag{7}$$

$$H = d/r, \tag{8}$$

$$X = (1+H)^2 + L^2, \tag{9}$$

$$Y = (1-H)^2 + L^2, \tag{10}$$

$$M = \sqrt{\frac{H-1}{H+1}}. \tag{11}$$

This method of calculation agrees well with radiometric measurements, both axially and radially, whereas a simple inverse square dependence overestimates the incident power at distances less than 10 cm [*Kowalski and Bahnfleth*, 2000]. The UV flux from the hemispheric end to the quartz finger was then added to the calculated flux from the cylinder using the inverse-square law. The walls of the Pyrex bulb were treated as perfect absorbers of UV light.

A schematic of the reaction bulb, with a contour plot of the modeled irradiance within the bulb, is shown in Figure 1. The irradiance decreased with distance from the quartz finger, from 15 to 20 mW at the surface to nearly zero at the wall. It reproduced the manufacturer-specified irradiance of 5400 μW at 1.9 cm using an initial UV flux of 5600 μW. To calculate the photon number density, the irradiance was integrated volumetrically within the bulb volume. The resulting average photon number density inside the bulb was 2.3×10^{15} photons $cm^{-3}\,s^{-1}$ at 254 nm (2.9×10^{15} photons $cm^{-3}\,s^{-1}$ with 80% transmission) and 2.6×10^{13} photons $cm^{-3}\,s^{-1}$ at 185 nm (3% of the flux at 254 nm with 30% transmission through quartz). These values are similar to those calculated for other experiments involving a mercury line source [*Wiegel et al.*, 2013], and they were used in the photochemical model without further adjustment.

3.2.2. Chemistry

To simulate the kinetics of the photochemical experiments, a reaction network for the O_2/O_3 photochemical system was built in KINTECUS [*Ianni*, 2003] using literature reaction rate coefficients and photolysis cross sections [*Yoshino et al.*, 1992; *Sander et al.*, 2011; *Wiegel et al.*, 2013]. Isotope exchange, ozone formation, and excited-state oxygen photochemistry, i.e., that involving $O(^1D)$, $O_2(^1\Delta)$, and $O_2(^1\Sigma)$, were included to model concentrations of $O(^3P)$ accurately (see Table 1). The relative chemical simplicity of the reaction system also allowed a thorough treatment of O_2 and O_3 isotopologues. In total, the model contained 321 reactions (see supporting information). A brief description of its major features follows.

The reactions with the most significant effects on Δ_{36} and Δ_{35} values are the isotope exchange reactions. Temperature-dependent rates of oxygen isotope exchange for $^{18}O(^3P) + {}^{16}O^{16}O$ and $^{16}O(^3P) + {}^{18}O^{18}O$ were taken from the combined theoretical-experimental study by *Fleurat-Lessard et al.* [2003] (3.4×10^{-12} $cm^3\,s^{-1}$ and 2.7×10^{-12} $cm^3\,s^{-1}$, respectively, at 300 K). These rate coefficients were consistent with results from other laboratory experiments [*Anderson et al.*, 1985b; *Wiegell et al.*, 1997]. The rates of $O(^3P) + O_2$ isotope exchange involving other isotopologues have not been directly predicted or measured, but the principle of microscopic reversibility allows one to derive relative rate coefficients based on equilibrium constants of each reaction. Relative $O(^3P) + O_2$ isotope exchange rate coefficients were therefore calculated using the reduced partition function ratios of the O_2 isotopologues involved in each reaction (see Table 2), similar to the method used in previous calculations [*Kaye and Strobel*, 1983; *Hathorn and Marcus*, 2000]. These relative rates are expected to yield the equilibrium isotopologue distributions for $^{18}O^{18}O$ (Δ_{36}) calculated in *Wang et al.* [2004]. An additional seven rate coefficients

Table 1. Reactions Families in Photochemistry Model[a]

Reaction	Rate Coefficient at 300 K	References and Notes
$O_2 + h\nu(185\,nm) \rightarrow O(^3P) + O(^3P)$	$1.0\times10^{-7}\,s^{-1}$	*Yoshino et al.* [1992]
$O_3 + h\nu\,(254\,nm) \rightarrow O_2(^1\Delta) + O(^1D)$	$0.9\times[2.7\times10^{-2}\,s^{-1}]$	*Sander et al.* [2011]
$\rightarrow O_2 + O(^3P)$	$0.1\times[2.7\times10^{-2}\,s^{-1}]$	*Sander et al.* [2011]
$Q - O + O(^3P) \rightarrow O_2 + Q(^3P)$	$3\times10^{-12}\,cm^3\,s^{-1}$	Average rate coefficient; see supporting information for isotopologue-specific rate coefficients.
$2O_2 + O(^3P) \rightarrow O_3 + O_2$	$6.0\times10^{-34}\,cm^6\,s^{-1}$	For $^{16}O^{16}O^{16}O$; see supporting information for isotopologue-specific rate coefficients from *Mauersberger et al.* [1999], *Schinke et al.* [2006], and *Gao and Marcus* [2007].
$O_3 + O(^3P) \rightarrow 2O_2$	$8.3\times10^{-15}\,cm^3\,s^{-1}$	*Sander et al.* [2011]
$O_3 + O(^1D) \rightarrow 2O_2$	$1.2\times10^{-10}\,cm^3\,s^{-1}$	*Sander et al.* [2011]
$\rightarrow O_2 + 2O(^3P)$	$1.2\times10^{-10}\,cm^3\,s^{-1}$	*Sander et al.* [2011]
$O_2 + O(^1D) \rightarrow O_2 + O(^3P)$	$0.2\times[4.0\times10^{-11}\,cm^3\,s^{-1}]$	*Sander et al.* [2011]
$\rightarrow O_2(^1\Sigma) + O(^3P)$	$0.8\times[4.0\times10^{-11}\,cm^3\,s^{-1}]$	*Sander et al.* [2011]
$O_2(^1\Delta) + O_2 \rightarrow 2O_2$	$1.7\times10^{-18}\,cm^3\,s^{-1}$	*Sander et al.* [2011]
$O_2(^1\Delta) + O_3 \rightarrow 2O_2 + O(^3P)$	$4.0\times10^{-15}\,cm^3\,s^{-1}$	*Sander et al.* [2011]
$O_2(^1\Sigma) + O_2 \rightarrow O_2(^1\Delta) + O_2$	$4.0\times10^{-17}\,cm^3\,s^{-1}$	*Sander et al.* [2011]
$O_2(^1\Sigma) + O_3 \rightarrow O_2(^1\Delta) + O_3$	$0.3\times[2.2\times10^{-11}\,cm^3\,s^{-1}]$	*Sander et al.* [2011]
$\rightarrow 2O_2 + O(^3P)$	$0.7\times[2.2\times10^{-11}\,cm^3\,s^{-1}]$	*Sander et al.* [2011]
$O_2(^1\Sigma) + O(^3P) \rightarrow O_2(^1\Delta) + O(^3P)$	$8.0\times10^{-14}\,cm^3\,s^{-1}$	*Sander et al.* [2011]

[a]A list of all isotopologue-specific reaction rates used in the model can be found in the supporting information. Here *Q* represents any stable isotope of oxygen.

are required to describe the remaining 14 reactions involving ^{17}O. For those reactions, we used nominal rate coefficients of $1.5\times10^{-12}\,cm^3\,s^{-1}$ for each product channel [e.g., $^{17}O(^3P) + {}^{16}O^{18}O \rightarrow {}^{16}O(^3P) + {}^{17}O^{18}O$]. For reactions with O_2 reactants that were homonuclear [e.g., $^{18}O(^3P) + {}^{17}O^{17}O \rightarrow {}^{17}O(^3P) + {}^{17}O^{18}O$], the two identical product channels summed to $3\times10^{-12}\,cm^3\,s^{-1}$. While the use of these nominal rate coefficients was a necessary approximation to model the kinetics of Δ_{35}, variations in them had a negligible effect on the modeled Δ_{36} and Δ_{35} kinetics when the coefficients were doubled or halved. A full quantum dynamical or transition state theory calculation of these rate coefficients is beyond the scope of this study, which focuses on quantities that depend mainly on the relative rates.

Isotopologue-specific O_3 formation rate coefficients, where available, were taken from *Mauersberger et al.* [1999]. The rate coefficients for the $^{16}O^{17}O^{18}O$-forming channels were derived from theoretical predictions [*Schinke et al.*, 2006; *Gao and Marcus*, 2007] because they were not measured by *Mauersberger et al.* [1999]. For simplicity, position-specific isotopic substitutions within O_3 molecules were not explicitly represented; no distinction was made between $^{18}O^{16}O^{16}O$ and $^{16}O^{18}O^{16}O$. While this treatment has important consequences for the isotopic enrichments in O_3, our experiments were conducted at low pressures (3–10 mbar), where little O_3 is formed. At these pressures, the mass balance favors O_2 by a factor of 10^4, and the rate of isotopic exchange is 10^5 times faster than that of O_3 formation. Furthermore, the production of molecular oxygen through other channels, e.g., O_3 photolysis, $O_2(^1\Delta) + O_3$, and $O(^1D) + O_3$, occurs at less than 5% the rate of $O(^3P) + O_2$ isotope exchange. The time evolution of Δ_{36} and Δ_{35} was therefore controlled by the $O(^3P)$ concentration and the rates of $O(^3P) + O_2$ isotope exchange.

Table 2. Isotope Exchange Equilibrium Constants at 300 K Used in Photochemistry Model

Reaction	$K_{eq,300K}$
$^{16}O(^3P) + {}^{17}O^{17}O \rightleftharpoons {}^{17}O(^3P) + {}^{16}O^{17}O$	1.9180
$^{16}O(^3P) + {}^{18}O^{18}O \rightleftharpoons {}^{18}O(^3P) + {}^{16}O^{18}O$	1.8463
$^{17}O(^3P) + {}^{16}O^{16}O \rightleftharpoons {}^{16}O(^3P) + {}^{16}O^{17}O$	2.0846
$^{17}O(^3P) + {}^{18}O^{18}O \rightleftharpoons {}^{18}O(^3P) + {}^{17}O^{18}O$	1.9259
$^{18}O(^3P) + {}^{16}O^{16}O \rightleftharpoons {}^{16}O(^3P) + {}^{16}O^{18}O$	2.1633
$^{18}O(^3P) + {}^{17}O^{17}O \rightleftharpoons {}^{17}O(^3P) + {}^{17}O^{18}O$	2.0762
$^{16}O(^3P) + {}^{17}O^{18}O \rightleftharpoons {}^{17}O(^3P) + {}^{16}O^{18}O$	0.9586
$^{16}O(^3P) + {}^{17}O^{18}O \rightleftharpoons {}^{18}O(^3P) + {}^{16}O^{17}O$	0.9238
$^{17}O(^3P) + {}^{16}O^{18}O \rightleftharpoons {}^{18}O(^3P) + {}^{16}O^{17}O$	0.9637

The experiment was treated as isothermal for two reasons. First, we calculated that heating of the gas in the bulb due to light absorption would be negligible, even in the absence of a thermal bath: The optical depth was always $< 10^{-3}\,cm^{-1}$ for O_3 and O_2, yielding $<10\,\mu W$ of light absorbed. Second, nearly all isotope exchange reactions should occur thermally because hyperthermal collisions, which would raise the

effective reaction temperature, are rendered insignificant by the rapid recycling of $O(^3P)$; of all the $O(^3P) + O_2$ collisions leading to isotope exchange events, those coming from nascent hyperthermal collisions are vanishingly few in number.

The low pressures in the reaction bulb also increase the importance of wall effects, but we expect gas phase isotope exchange reactions to dominate the isotopic ordering signal during the relatively short (<1 h) experiments described here. The mean free path of $O(^3P)$ is $< 225\ \mu m$ at 300 K ($Z = 8 \times 10^5\ s^{-1}$) and approximately one out of thirty $O(^3P) + O_2$ collisions results in isotope exchange. In addition, previous studies suggest that the $O + O_2$ recombination efficiency on Pyrex is < 1% above 100 K, with quenching of excited O_3^* on walls being orders of magnitude less likely [*Macko et al.*, 2004; *Janssen and Tuzson*, 2010]. Nonetheless, both of these effects would increase the effective rate of O_3 formation, leading to enhanced photolytic generation of atomic oxygen. Recombination of two oxygen atoms to form O_2 is expected to be negligible because of low atomic oxygen concentrations. In summary, the net effect of wall-assisted recombination reactions should be negligible; however, they could increase the rate of gas phase isotopic reordering by increasing $O(^3P)$ concentrations slightly.

3.3. Analytical Methods

Our analytical procedures were modified slightly from those described in *Yeung et al.* [2012]. To analyze the isotopologues of O_2, samples containing 150–200 μmol of O_2 were passed through a gas chromatograph purification system (GC; molecular sieve 5A column, 3 m × 1/8 inch OD) at −80°C to remove N_2 and Ar. The ultrahigh-purity helium carrier gas used for this system (99.9995%) was further purified by passing it through a silica gel column (6 feet × 1/8 inch OD) and a molecular sieve 5A U-trap, both of which were immersed in liquid nitrogen. After the GC separation, the purified O_2 was adsorbed onto a molecular sieve adsorbent at −196°C, transferred to an isotope ratio mass spectrometer (IRMS; ThermoFinnigan MAT 253), and analyzed for its isotopic composition against a working reference gas (m/z = 32–36). Standard gases were then purified and measured over a range of Ar concentrations to obtain ion-correction relationships for the ^{36}Ar-$^{18}O^{18}O$ isobaric interference. The residual Ar content of the sample was measured by peak-hopping to obtain the voltage (i.e., ion current) compared with that of the standard ($V_{40,SA}/V_{40,ST}$) at three separate times during the 5 h analysis time (90–120 sample standard comparison cycles with 10 s per individual integration and a 25 s preintegration delay). The inferred ^{36}Ar concentration of the sample was then used to correct the measured m/z = 36 ion beam for interfering ^{36}Ar (about 7–18 mV out of 400 mV total). The IRMS procedures are described in detail in *Yeung et al.* [2012] and in Appendix A. This analytical method yields Δ_{36} and Δ_{35} values with a precision of $1\sigma \sim \pm 0.1$‰ and ± 0.2‰, respectively, at a rate of two analyses (one sample and one standard) per day. Precision for $\delta^{18}O$ and $\Delta^{17}O$ with this method are ±0.04‰ and 5 ppm, respectively [*Young et al.*, 2014].

The measurements were standardized against gases generated using the reversible decomposition of BaO_2 powder at 800°C:

$$2BaO_{2(s)} \rightleftharpoons 2BaO_{(s)} + O_{2(g)}, \tag{12}$$

The resulting O_2 gas is at high-temperature isotopic equilibrium (Δ_{36} = 0.03‰ and Δ_{35} = 0.02‰ at 800°C) [*Wang et al.*, 2004], thus resembling the stochastic distribution used to define Δ_n values. The O_2 produced from BaO_2 is low in Ar because O_2 evolves exclusively from the lattice when the peroxide is heated above 600°C [*Tribelhorn and Brown*, 1995]. Additional high-temperature standards were generated by heating O_2 gas to 1000°C with platinum wire, which catalytically equilibrates oxygen isotopes in O_2. These standards are used to correct for bulk composition-dependent nonlinearities on the IRMS.

Isotopic ordering was quantified by (1) comparing the measured Δ_{36} and Δ_{35} values against the BaO_2 standard-derived ion correction and then (2) making a correction for the difference in bulk isotopic composition between standards and the unknown. These corrections are arithmetic corrections that were detailed in an earlier publication [*Yeung et al.*, 2012]; long-term drifts in Ar content of the reference gas were corrected using the model described in Appendix A.

3.4. Experimental Results

Photochemical isotopic reordering occurred within several minutes inside the reaction bulb, with values of Δ_{36} and Δ_{35} reaching a steady state within 5 min at 300 K. This rapid temporal evolution of Δ_{36} and Δ_{35} was reproduced by the photochemical model without altering any of the input parameters (see Figure 2). The

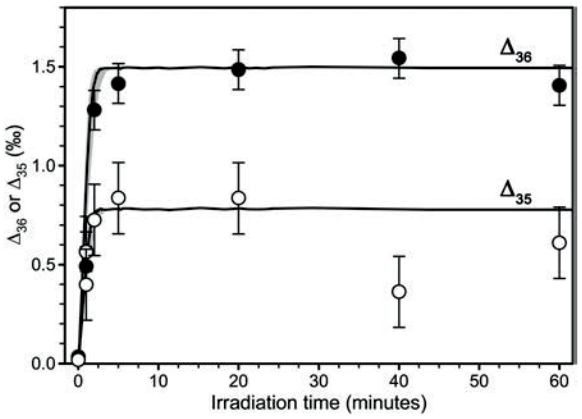

Figure 2. Agreement between experimental and modeled photochemical kinetics of isotopic ordering at 300 K. Measured Δ_{36} and Δ_{35} values (black and white circles, respectively) are plotted according to cumulative irradiation time. The modeled temporal evolution described in the text is shown as black curves. Shaded areas depict the range in reordering rate that would result from a ±30% change in photon number density. Steady state Δ_{36} and Δ_{35} values were approached regardless of starting values (see Table 3). Uncertainties shown are assumed $\pm 1\sigma$ based on external reproducibility of measurements.

calculated isotope exchange rates also yielded near-quantitative agreement between the experimental and the modeled steady state values at 300 K. Concentrations of other oxygen-containing species were kept low during these short experiments: Typical modeled concentrations at 300 K were $[O_3] \leq 2 \times 10^{13}$ cm^{-3}, $[O(^1D)] \leq 10^5$ cm^{-3}, and $[O(^3P)] \leq 10^{11}$ cm^{-3}, compared with O_2 number densities of 10^{17} cm^{-3}.

The excellent agreement between the experiments and the model, for both Δ_{36} and Δ_{35}, supports our hypothesis that $O(^3P) + O_2$ isotope exchange reorders the isotopes in O_2. Changes to the rates of the other reactions have no significant effect on the modeled values of isotopic ordering; only changes to the photon number density or the relative rates of isotope exchange altered the temporal evolution of Δ_{36} and Δ_{35}. For example, excluding excited-state $O_2(^1\Sigma)$ chemistry slows the model's approach to steady state by ~15% and leaves the steady state Δ_{36} and Δ_{35} values nearly unchanged. To test the sensitivity of the model to irradiance, we simulated the temporal evolution of Δ_{36} and Δ_{35} for photon number densities ±30% about the a priori value of 2.3×10^{15} photons cm^{-3} s^{-1} (254 nm) and 2.6×10^{13} photons cm^{-3} s^{-1} (185 nm) calculated in section 3.2.1; the kinetics of the first several minutes of photolysis varied somewhat, but steady state values of isotopic ordering were reached within 5 min in all irradiance scenarios (see Figure 2).

Temperature variations are expected to have little effect on the overall kinetics of the laboratory experiments (although they affect the steady state Δ_{36} and Δ_{35} values). While O_3 formation is faster at lower temperatures, the low pressures in the reaction vessel favor isotope exchange by at least a factor of 10^5 between 200 K and 400 K. Over this temperature range, we calculate that Δ_{36} and Δ_{35} reached steady state values within 10 min. The temperature of the quartz finger also reached a steady state after ~10 min. For the kinetics experiments described above, this initial warming of the quartz finger resulted in an uncertainty in the mean gas temperatures, T_{gas}, of ±2 K. For experiments maintaining a steady state for at least 10 min, the uncertainty in the mean gas temperature is also ± 2 K, limited by the stability of the bath temperature.

Photolysis experiments, conducted for at least 40 min, had steady state Δ_{36} and Δ_{35} values that varied inversely with temperature. These steady state Δ_{36} and Δ_{35} values were similar to those predicted for isotopic equilibrium by ab initio calculations (see Table 3) [*Wang et al.*, 2004]. However, while we observed good agreement between steady state and predicted equilibrium isotopic ordering at $T > 300$ K, the steady state values for Δ_{36} and Δ_{35} at $T < 300$ K were consistently lower than those predicted by theory (see Figure 3).

Despite this apparent disagreement between experiment and theory, we argue here that the experimental steady state values are true steady states that represent isotopic equilibrium. First, we conducted photolysis experiments in which the O_2 sample was irradiated for 6 and 24 h in a −78°C bath (218 K gas temperature) to determine if longer irradiation times resulted in an isotopic order closer to equilibrium. The resulting Δ_{36} and Δ_{35} values were indistinguishable from experiments lasting 40 min. Second, the steady state Δ_{36} and Δ_{35} values did not depend on the starting values: Experiments in which O_2 was reordered from high Δ_{36} and Δ_{35} values to lower Δ_{36} and Δ_{35} values yielded steady state isotopic ordering that was indistinguishable from samples that were reordered starting at Δ_{36}, Δ_{35} ~0 (see Table 3). This behavior was reproduced in the photochemical model. Third, our analytical corrections yielded consistent Δ_{36} values over a 5 month period; for example, experiments with O_2 spanning 34‰ in $\delta^{18}O$ yielded steady state Δ_{36} values within ~0.1‰ during that time. The invariance of isotopic ordering, despite all these perturbations to the photochemical experiments and analyses, suggests that our 40 min photolysis experiments yielded a distribution of O_2 isotopologues that closely resembles isotopic equilibrium.

Table 3. Photochemical Data for Steady State Experiments

T_{bath}/°C	T_{finger}/°C	T_{gas}/K	$\Delta_{36,measured}$	$\Delta_{35,measured}$	$\Delta_{36,theory}$	$\Delta_{35,theory}$	Notes
				1 × GC			
88	92	361.4	0.96	0.52	1.00	0.52	
91	110	365.9	0.98	0.29	0.97	0.51	
25	68	302.2	1.43	0.36	1.48	0.77	
25	70	302.2	1.37	0.60	1.48	0.77	
25	64	301.6	1.34	0.62	1.48	0.78	
25	73[a]	302.6	1.54	0.33	1.47	0.77	Photolyzed 6 h
−34	72	252.7	1.97	0.99	2.08	1.08	From high initial Δ_{36}, Δ_{35}
−77	60	218.6	2.51	1.28	2.66	1.39	
−77	60	218.6	2.29	1.30	2.66	1.39	
−77	60	218.6	2.36	0.90	2.66	1.39	Photolyzed 24 h
−77	60	218.6	2.42	1.20	2.66	1.39	Photolyzed 6 h
−97	62	206.7	2.57	1.39	2.91	1.52	
				2 × GC			
800	-	1073.1	0.55	0.03	0.03	0.02	No photolysis
800	-	1073.1	0.56	0.18	0.03	0.02	No photolysis
800	-	1073.1	0.43	−0.10	0.03	0.02	No photolysis
90	116	365.7	1.16	0.76	0.97	0.51	
91	118	366.4	1.18	0.97	0.50	0.51	
25	72	302.4	1.52	0.60	1.47	0.77	
25	92	304.8	1.54	0.52	1.45	0.76	
−35	72	252.0	1.90	0.90	2.09	1.09	
−35	72	252.0	1.93	1.15	2.09	1.09	
−77	60	218.6	2.26	1.31	2.66	1.39	
−77	62	219.1	2.24	1.03	2.65	1.38	
				Additional Tests (1 × GC)			
25	-	298.0	1.43	0.64	1.52	0.79	From high initial Δ_{36}, Δ_{35}[b]
25	81	303.5	1.25	0.95	1.46	0.77	$\delta^{18}O = -36‰$[c]
25	73[a]	302.4	1.31	0.77	1.47	0.77	$\delta^{18}O = -36‰$[c]

[a] T_{finger} not measured directly; presumed to be equal to mean value for this T_{bath}.
[b] Catalyzed by photolysis of O_3 in ambient light over a period of 2 months.
[c] Relative to atmospheric O_2. $\delta^{18}O$ of O_2 used in photochemical experiments was ~−2‰.

If the photochemical reordering indeed yields equilibrium isotopic ordering, then only two mechanisms can explain the disagreement between experimental and theoretical Δ_{36} and Δ_{35} values: Either (1) the theoretical predictions overestimate isotopic ordering at equilibrium or (2) isotopic reordering is occurring during sample purification. While the theoretical predictions were based on the reduced harmonic partition function ratios, they are benchmarked by spectroscopic measurements, which suggest that anharmonic effects on the partition function would not be detectable at the current level of analytical precision ($\sigma \sim 0.1‰$) [*Robichaud et al.*, 2009]. We hypothesize, therefore, that isotopic reordering occurred during sample purification.

The absence of significant reordering during IRMS analysis and upon simple adsorption/desorption on the molecular sieve transfer fingers [*Yeung et al.*, 2012] implicates the GC column as the site of isotopic reordering. To test this hypothesis, we compared the isotopic ordering of samples passed once through the GC column to those passed twice through the GC column. If reordering occurs on the GC column, samples passed twice through should exhibit departures from equilibrium values that are twice as large as those for single-pass samples. Indeed, two-pass samples appeared more reordered than one-pass samples: Δ_{36} values of O_2 reordered at low temperatures were even lower after a second pass through the GC. In addition, high-temperature samples showed elevated Δ_{36} values, indicating that O_2 was being reordered toward a common measured value ($\Delta_{36} \sim 1.8‰$) on the GC column. In contrast, isobaric interferences at $m/z = 36$ would only elevate Δ_{36} values (see Appendix A) instead of simultaneously depressing high Δ_{36} values and elevating low Δ_{36} values. These data suggest that the GC column catalyzed partial isotopic reordering, perhaps due to transition-metal impurities present on the molecular sieve 5A zeolite [*Biermann and Janssen*, 1989; *Starokon et al.*, 2011]. Subsequent removal of the molecular sieve U-trap that was directly upstream of the GC system significantly improved isotopic ordering fidelity in several new GC columns that were installed after the data in this manuscript were

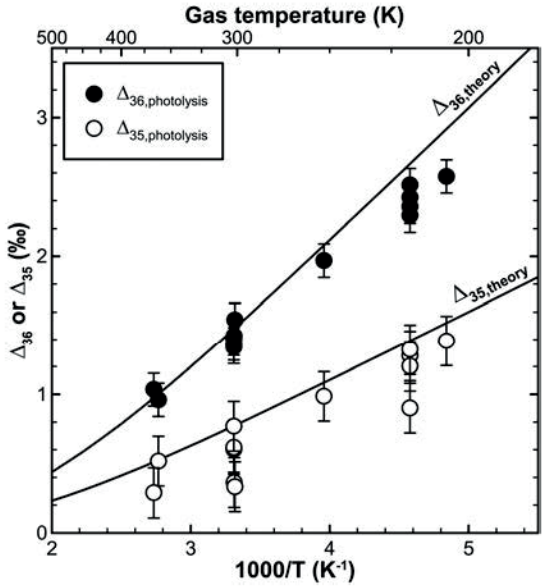

Figure 3. Inverse relationship between temperature (T_{gas}) and Δ_{36} and Δ_{35} values at steady state. Experimental steady state values $\Delta_{36,photolysis}$ and $\Delta_{35,photolysis}$ values (black and white circles, respectively) are compared to calculated Δ_{36} and Δ_{35} values at isotopic equilibrium (black curves). Generally, good agreement between experiment and theory is observed, but $\Delta_{36,photolysis}$ is consistently lower than $\Delta_{36,theory}$ at low temperatures. This discrepancy is attributed to heterogeneous reordering during sample purification (see section 3.4). Uncertainties shown are assumed $\pm 1\sigma$ based on external reproducibility of measurements.

collected. Furthermore, deliberate "poisoning" of one of those columns resulted in reordering that resembled the reordering reported here. We therefore hypothesize that some activating impurities had been transferred from the U-trap to the GC columns used in this study to cause partial O_2 isotope reordering.

Plotting theoretical Δ_{36} values against experimental values revealed the amount of reordering during each GC column pass. In such a plot, zero reordering would yield a slope of unity and an intercept of zero. Reordering toward $\Delta_{36} \sim 1.8‰$ would result in a slope greater than unity and an intercept less than zero. For both single-GC and double-GC analyses, we observed a slope greater than unity and an intercept less than zero (Figure 4). Experimental and theoretical values are highly correlated in both cases. The magnitude of the slopes indicated isotopic reordering of ~20% per pass on the GC column ($d\Delta_{36,theory}/d\Delta_{36,photolysis} = 1.18 \pm 0.08$; 2σ), and they are consistent with a doubling of isotopic reordering upon a second pass through the GC column ($d\Delta_{36,theory}/d\Delta_{36,photolysis} = 1.49 \pm 0.06$; 2σ). Reordering was neither observed unequivocally nor ruled out in Δ_{35} values because of the smaller reordering signature expected (roughly half the magnitude observed in Δ_{36}) and the higher relative uncertainty in those measurements. From these data, we infer that the Δ_{36} and Δ_{35} values at steady state were near the theoretically predicted isotopic equilibrium values.

The preceding experimental results show that (1) only $O(^3P) + O_2$ isotope exchange can explain the kinetics of Δ_{36} and Δ_{35} evolution and (2) the isotopic steady state is indistinguishable from isotopic equilibrium. The supporting data are consistent over a 5 month period, across several working-standard reference gases, GC columns, and IRMS tuning settings, indicating that analytical biases are unlikely. We conclude that $O(^3P) + O_2$ isotope exchange drives the isotopic order of O_2 to isotopic equilibrium.

4. Measurements of Atmospheric O_2 From 2012 to 2014

Photochemical equilibration of O_2 can be used to calibrate measurements of Δ_{36} and Δ_{35} in natural O_2 samples (e.g., Figure 4). We used this calibration method to refine the Δ_{36} and Δ_{35} values in atmospheric O_2, which our lab first reported in 2012. Over 14 months, samples of air (25 cm^3) were collected, between 7 and 10 A.M., in the UCLA Court of Sciences and prepared and analyzed according to the method described above. The high initial Ar content, however, required a second pass through the GC column to reduce residual ^{36}Ar to the working range of ~10 ppb. We therefore used the relationship between $\Delta_{36,photolysis}$ and $\Delta_{36,theory}$ for two GC passes (see Figure 4) to correct measured values of Δ_{36} for isotopic reordering on the GC column and the corresponding relationship to correct the measured values of Δ_{35}. The ±2°C uncertainty in T_{gas} (primarily from T_{bath}) contributed ~0.02‰ uncertainty to Δ_{36} and ~0.01‰ uncertainty in Δ_{35}.

Values of Δ_{36} and Δ_{35} showed no detectable drift during over 14 months. In addition, a Shapiro-Wilk normality analysis of the data indicates that they are consistent with a normal distribution about their respective means, with $\sigma_{\Delta 36} = 0.17‰$ and $\sigma_{\Delta 35} = 0.3‰$ ($p = 0.5$ and 0.3, respectively; see Figure 5). These standard deviations are similar to those observed for the calibration standards (e.g., $\sigma_{\Delta 36} = 0.1‰$), although the second pass through the GC likely decreased the reproducibility slightly. Mean values of isotopic order in UCLA air derived from this data

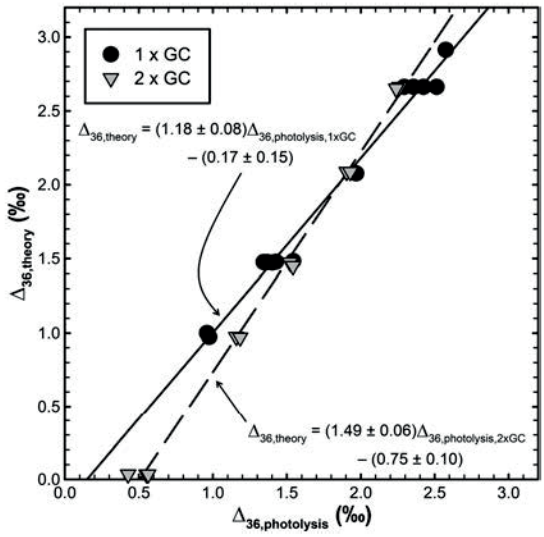

Figure 4. Quantifying isotopic reordering on the GC column for experimental Δ_{36} calibration. Theoretical values of Δ_{36} at isotopic equilibrium ($\Delta_{36,theory}$) are plotted against measured Δ_{36} values from steady state photochemical experiments passed once (black circles) and twice (grey triangles) through the GC column, along with the best fit lines and 2σ uncertainties in the fits. Zero reordering on the GC column would result in a slope of 1 and intercept of zero. Instead, the data show slopes greater than zero and intercepts less than zero, suggesting partial reordering upon each GC pass.

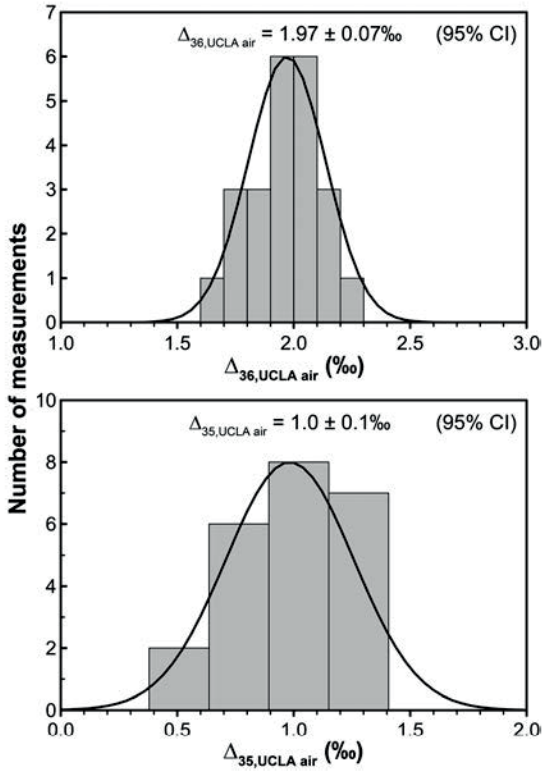

Figure 5. Histograms of calibrated Δ_{36} and Δ_{35} values of UCLA air measured over 14 months. Shown also are mean values and 95% confidence intervals.

set were $\Delta_{36} = 1.97 \pm 0.07$‰ and $\Delta_{35} = 1.0 \pm 0.1$‰ (2 s.e.; $n = 23$). These values of isotopic ordering in atmospheric O_2 are consistent with the values we reported previously, which had threefold to fourfold greater uncertainty.

The improved precision in the new data reported here reveal that the air sampled at UCLA is out of equilibrium with the annual mean local temperature (290 K), the annual mean global surface temperature (288 K), and also the annual mean midtropospheric temperature at ~5.5 km ($T_{trop} = 252$ K) [*Vinnikov and Grody*, 2003; *Vinnikov et al.*, 2006], which could not be ruled out in our earlier study. The effective equilibrium temperature corresponding to our reported atmospheric Δ_{36} value is 260 ± 5 K, and the probability that it corresponds to T_{trop} is $p < 0.01$.

5. Discussion

These data bolster the case that isotopic ordering in O_2 is altered by $O(^3P) + O_2$ isotope exchange reaction throughout the atmosphere. High $O(^3P)$ concentrations in the stratosphere, for example, will rapidly reorder the isotopes in O_2 there (see Figure 6) [*Anderson*, 1975; *Anderson et al.*, 1985a; *Brasseur and Solomon*, 2005]. The kinetic rate coefficients for isotope exchange, which were verified in this study, further imply that the time scale of the reordering ranges from months to days, depending on altitude and attendant $O(^3P)$ concentration. The low temperatures in the stratosphere should result in reordering to high Δ_{36} and Δ_{35} values (≥ 2.5‰ and ≥ 1.3‰, respectively) before that air returns to the troposphere several years after entering the stratosphere [*Holzer et al.*, 2012; *Orbe et al.*, 2012]. Yet the measured tropospheric Δ_{36} and Δ_{35} values are significantly lower, implying reordering upon descent to ground level.

Isotopic ordering in the troposphere therefore represents a dynamic balance of physical and chemical influences: High Δ_{36} and Δ_{35} stratospheric air mixes continuously into the troposphere at a rate of $1–5 \times 10^{18}$ mol O_2 yr^{-1} (the net O_2 flux depends on the precise definition of the tropopause) [*Holton et al.*, 1995; *Appenzeller et al.*, 1996; *Yang and Tung*, 1996; *Schoeberl*, 2004; *Škerlak et al.*, 2014], so some form of chemical reordering is required to explain the lower Δ_{36} and Δ_{35} values observed in tropospheric air. This reordering mechanism must (1) drive isotopic ordering toward low Δ_{36} and Δ_{35} values and

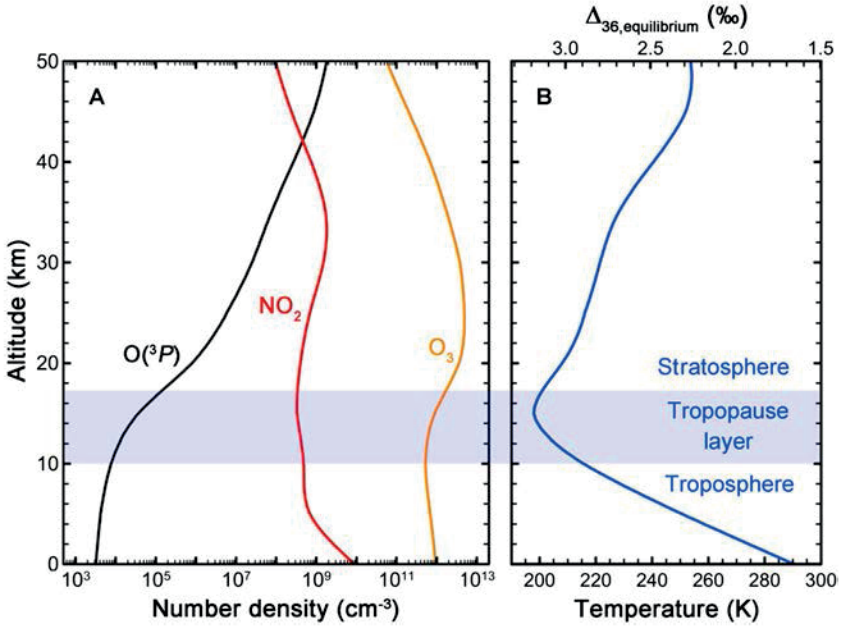

Figure 6. Atmospheric vertical profiles of (a) $O(^3P)$ and its main precursors NO_2 and O_3 and (b) temperature. Plots shown are globally and seasonally averaged outputs from the model of *Brasseur et al.* [1990], so the meridional variation in tropopause height is not apparent. The shaded layer in this plot therefore represents the range in tropopause heights, from ~ 17 km in the tropics to 8–10 km at the poles in winter. Net stratosphere-to-troposphere mass exchange occurs primarily in the extratropics, where the tropopause is ~12 km [*Orbe et al.*, 2012].

(2) occur rapidly enough to balance the stratosphere-to-troposphere flux of Δ_{36} and Δ_{35}. Biological cycling of O_2 is likely of limited importance, for example, because it is too slow by several orders of magnitude to counter the influence of stratospheric air mixing into the troposphere [*Blunier et al.*, 2002].

Tropospheric $O(^3P)$ concentrations, in contrast, may be high enough to reorder O_2 to tropospheric values on the necessary time scales: The tropospheric trace gases NO_2 and O_3 both photolyze to produce $O(^3P)$, while the $O(^3P) + O_2$ isotope exchange reaction proceeds quickly with no net consumption of that $O(^3P)$. Measured Δ_{36} and Δ_{35} values would then place constraints on where this isotope exchange chemistry must occur. Within ~5 km of the surface, typical daytime temperatures ($T_{trop} > 260$ K) are warm enough for photochemistry to drive isotopic ordering to the observed Δ_{36} and Δ_{35} values. At altitudes $\geq$5 km, however, photochemical isotope reordering would yield Δ_{36} and Δ_{35} values that are too high because the temperatures at those altitudes are too cold ($T_{trop} < 260$ K). Therefore, to explain the Δ_{36} and Δ_{35} values of tropospheric O_2, photochemical isotope reordering at low altitudes must presently outpace isotopic reordering at higher altitudes in the troposphere.

Intraannual and latitudinal variations in Δ_{36} and Δ_{35} may not be detectable at the current precision, especially if tropospheric isotope reordering in O_2 occurs on time scales much longer than the 1–2 year time scale tropospheric mixing [*Waugh et al.*, 2013]. Using the annual rates of gas phase O_2 reordering and stratosphere-troposphere mass exchange, combined with first-order estimates of $O(^3P)$ concentrations in the troposphere ($\leq$5000 cm^{-3}), the box model for Δ_{36} described by *Yeung et al.* [2012] indicates that isotopic ordering in atmospheric O_2 can vary on decadal time scales. However, the current null result does not rule out variations in isotopic ordering within the troposphere. Additional measurements of O_2 from different altitudes and latitudes as well as measurements of biological isotope fractionation will further constrain the balance of mechanisms yielding the present value of and potential atmospheric variations in O_2 isotopic ordering.

6. Conclusions

We have demonstrated that $O(^3P) + O_2$ isotope exchange reactions rapidly reorder the isotopes in O_2 to equilibrium. We found that UV irradiation of pure O_2 yields steady state isotopic enrichments in $^{18}O^{18}O$

and $^{17}O^{18}O$ that agree with theoretical predictions over a range of temperatures. This photochemistry forms the core of a robust and precise method to calibrate measurements of isotopic ordering in O_2, i.e., Δ_{36} and Δ_{35}. While some isotopic reordering can occur during sample purification, the extent of reordering can be routinely quantified and corrected, as demonstrated by the long-term stability of the calibration and of tropospheric air measurements at UCLA.

The photochemical scheme described here provides an invaluable and rigorous link between theoretical predictions and laboratory measurements of isotopic ordering in O_2. Moreover, it can be replicated easily in different laboratory settings and interfaced with different measurement techniques. Thus, the photolysis scheme described here constitutes a practical standardization technique for future studies of O_2 in the fields of biogeochemistry, atmospheric chemistry, and quantitative spectroscopy. At present, the method's accuracy is primarily limited by uncertainties arising from sample processing and analysis, and to a lesser extent, the accuracy of the modeled in situ reaction temperature. Future refinements of the photochemical scheme will concentrate on minimizing internal temperature gradients and removing residual ozone for long-term storage. Improvements in mass spectrometric resolution should reduce long-term analytical uncertainties by reducing the amount of sample handling required.

The kinetics of the $O(^3P) + O_2$ isotope exchange reaction have significant implications for the interpretation of Δ_{36} and Δ_{35} values in nature. Ground-state atomic oxygen is ubiquitous in the atmosphere, so isotopic reordering via $O(^3P) + O_2$ likely controls isotopic ordering in O_2 wherever gas phase photochemistry is important. In restricted and aqueous environments, where $O(^3P)$ is not generated, other bond-altering processes will dominate. For example, photosynthetic water splitting and respiratory O_2 consumption, which are irreversible redox processes, should yield unique and likely nonequilibrium signatures on the generated and residual O_2, respectively. Isotopic ordering offers a window into the chemical physics of these processes as well as their contributions to the mass balance of O_2 in natural environments.

Appendix A: Ion Corrections

Empirical ion corrections are used in a variety of isotopologue analysis [*Huntington et al.*, 2009; *He et al.*, 2012; *Yeung et al.*, 2012; *Stolper et al.*, 2014], but they have scarcely been investigated in depth. The ion corrections in O_2 isotopologue analysis are especially challenging, so we present a model here that serves as a template for generating similar corrections in other systems.

Our previous work identified two main sources of unwanted ion current at the mass spectrometer's $m/z = 36$ Faraday cup: $^{36}Ar^+$ and a peak tail from other O_2^+ isotopologues. Measurements of ^{40}Ar were used as a proxy for ^{36}Ar content, specifically the voltage ratio between ^{40}Ar in the sample and in the laboratory working standard, i.e., $V_{40,SA}/V_{40,ST}$. This ratio can be measured precisely, but it is susceptible to long-term drift when the Ar content of the laboratory working-standard changes. Chemical fractionation and atmospheric leaks, which occurred during the expansion of daily standard aliquots into the IRMS bellows, yielded noticeable drift in the ion correction over time scales of weeks or longer. An expression for the dependence of Δ_{36} on $V_{40,ST}$ was therefore derived to model this behavior. By defining the measured $m/z = 36$ voltage as the sum of $^{18}O^{18}O^+$ and $^{36}Ar^+$ contributions, i.e., $V_{36} = V_{36O2} + V_{36Ar}$, the resulting 36/32 isotopologue ratio, $^{36}R_{measured}$, becomes

$$^{36}R_{\text{measured}} = \left[\frac{\left(V_{36O2,SA} + V_{36Ar,SA}\right) / V_{32,SA}}{\left(V_{36O2,ST} + V_{36Ar,ST}\right) / V_{32,ST}}\right], \tag{A1}$$

where the subscript numbers refer to cardinal masses of each species and SA and ST refer to sample and standard, respectively. The stochastic 36/32 isotopologue ratio, $^{36}R_{stochastic}$, is calculated from the 34/32 isotopologue ratio, which is accurate to ~2 ppm when all $m/z = 34$ signal is assumed to be $^{16}O^{18}O$:

$$^{36}R_{\text{stochastic}} \approx \left[\frac{\left(V_{34,SA} / V_{32,SA}\right)}{\left(V_{34,ST} / V_{32,ST}\right)}\right]^2. \tag{A2}$$

Finally, we substitute $V_{36Ar} = kV_{40}$, where k is a proportionality factor accounting for both the relative $^{36}Ar/^{40}Ar$ abundance and instrumental mass fractionation effects. After imposing the laboratory pressure-balancing condition, i.e., $V_{32,SA} = V_{32,ST}$, the equation reduces to

$$\Delta_{36,\text{measured}} = \left[\frac{kV_{40,ST}}{V_{36O2,ST} + kV_{40,ST}}\left(\frac{V_{34,ST}}{V_{34,SA}}\right)^2\right]\left(\frac{V_{40,SA}}{V_{40,ST}}\right) + \left[\frac{V_{36O2,SA}}{V_{36O2,ST} + kV_{40,ST}}\left(\frac{V_{34,ST}}{V_{34,SA}}\right)^2 - 1\right]. \quad \text{(A3)}$$

Equation (A3) defines a line relating two measured quantities, $\Delta_{36,\text{measured}}$ and $V_{40,SA}/V_{40,ST}$, with a slope and intercept that depend on (1) the ^{40}Ar content of the working-standard gas and the (2) bulk $\delta^{18}O$ composition. As $V_{40Ar,ST}$ increases, the magnitude of both the slope and intercept increases. They also vary inversely with $V_{34,SA}/V_{34,ST}$, the bulk isotopic composition. These variations are approximately linear over the range of $V_{40,ST}$ we have measured.

Consideration of the ^{36}Ar isobar alone, however, is insufficient to account for the laboratory data; a peak tail and/or another isobar (e.g., $H^{35}Cl$) may be important. By casting $V_{36} = V_{36O2} + V_{36Ar} + V_{tail}$, equation (A3) becomes

$$\Delta_{36,\text{measured}} = \left[\frac{kV_{40,ST}}{V_{36O2,ST} + kV_{40,ST} + V_{tail,ST}}\left(\frac{V_{34,ST}}{V_{34,SA}}\right)^2\right]\left(\frac{V_{40,SA}}{V_{40,ST}}\right) + \left[\frac{V_{36O2,SA} + V_{tail,SA}}{V_{36O2,ST} + kV_{40,ST} + V_{tail,ST}}\left(\frac{V_{34,ST}}{V_{34,SA}}\right)^2 - 1\right]. \quad \text{(A4)}$$

The form of equation (A4) is similar to that of equation (A3), but with one notable difference: The intercept of the $\Delta_{36,\text{measured}}$ versus $V_{40,SA}/V_{40,ST}$ plot varies directly with $V_{tail,SA}$. Note that the dependence of the $\Delta_{36,\text{measured}}$ versus $V_{40,SA}/V_{40,ST}$ plot on bulk isotopic composition is weak; a peak tail from other O_2 isotopologues that depends on the bulk isotopic composition (i.e., $V_{tail,SA}$ increases with $V_{34,SA}$) would amplify that dependence. Indeed, we observed a dependence of the $\Delta_{36,\text{measured}}$ versus $V_{40,SA}/V_{40,ST}$ intercept on bulk isotopic composition, suggesting that this additional correction is justified [*Yeung et al.*, 2012].

To account for drift in $V_{36Ar,ST}$ and $V_{tail,SA}$ simultaneously, two types of standard gases were measured consistently during analytical sessions. First, high-temperature standards generated from BaO_2 decomposition were measured over a range of $V_{40,SA}/V_{40,ST}$ values. Probing a large range in $V_{40,SA}/V_{40,ST}$ over time allows one to monitor the changing slope and intercept of a $\Delta_{36,\text{measured}}$ versus. $V_{40,SA}/V_{40,ST}$ plot. Second, high-temperature standards generated by heating working-standard O_2 to 1000°C were measured. These secondary standards had $\delta^{18}O$ values different from those generated by BaO_2 decomposition; measuring Δ_{36} at two different $\delta^{18}O$ values allows one to account for bulk composition-dependent nonlinearities.

We allowed the slope and intercept of equation (A4) to evolve linearly with time, constrained by the BaO_2-derived standards. To arrive at a best fit time evolution of the slope and intercept, we varied the slope and intercept values at the beginning and end of each analytical period (four variables) such that the sum of squared deviations from the BaO_2-derived standards was minimized over the entire period. The resulting linear trends yielded a slope and intercept for each day of an analytical run; these parameters were used for the ion correction for all analyses conducted on that day. One check for the consistency of this method over time was the secondary standards (working-standard O_2 heated to 1000°C). Values of Δ_{36} of the secondary standards showed consistent deviations from the primary BaO_2-derived $\Delta_{36,\text{measured}}$ versus $V_{40,SA}/V_{40,ST}$ lines, confirming the presence of bulk composition-dependent nonlinearities. Gases with lower $\delta^{18}O$ had higher $\Delta_{36,\text{measured}}$ values, whereas gases with higher $\delta^{18}O$ had lower $\Delta_{36,\text{measured}}$ values, compared to the BaO_2-derived standards. These departures were constant over the course of analytical periods, when the IRMS source tuning parameters and ion optics remained unchanged. Both sets of standards displayed similar external standard deviations about the mean of 0.1–0.2‰.

Acknowledgments
We would like to thank E.A. Schauble and L.T. Murray for helpful discussions during the course of this work, and two anonymous reviewers and the Associate Editor for comments that improved the manuscript. This research was supported in part by the National Science Foundation (EAR-1049655 and DGE-1144087), the National Aeronautics and Space Administration Cosmochemistry program, and the Deep Carbon Observatory. The data and the model used to support the arguments made in this paper are freely available as supporting information.

References

Anderson, J. G. (1975), The absolute concentration of $O(^3P)$ in Earth's stratosphere, *Geophys. Res. Lett.*, *2*(6), 231–234, doi:10.1029/GL002i006p00231.

Anderson, J. G., N. L. Hazen, B. E. McLaren, S. P. Rowe, C. M. Schiller, M. J. Schwab, L. Solomon, E. E. Thompson, and E. M. Weinstock (1985a), Free radicals in the stratosphere: A new observational technique, *Science*, *228*(4705), 1309–1311.

Anderson, S. M., F. S. Klein, and F. Kaufman (1985b), Kinetics of the isotope exchange reaction of ^{18}O with NO and O_2 at 298 K, *J. Chem. Phys.*, *83*(4), 1648–1656.

Anderson, S. M., D. Hülsebusch, and K. Mauersberger (1997), Surprising rate coefficients for four isotopic variants of $O+O_2+M$, *J. Chem. Phys.*, *107*(14), 5385–5392.

Angert, A., S. Rachmilevitch, E. Barkan, and B. Luz (2003), Effects of photorespiration, the cytochrome pathway, and the alternative pathway on the triple isotopic composition on atmospheric O_2, *Global Biogeochem. Cycles*, *17*(1), 1030, doi:10.1029/2002GB001933.

Appenzeller, C., J. R. Holton, and K. H. Rosenlof (1996), Seasonal variation of mass transport across the tropopause, *J. Geophys. Res.*, *101*(D10), 15,071–15,078, doi:10.1029/96JD00821.

Bender, M., T. Sowers, and L. Labeyrie (1994), The Dole effect and its variations during the last 130,000 years as measured in the Vostok ice core, *Global Biogeochem. Cycles*, *8*(3), 363–376, doi:10.1029/94GB00724.

Biermann, J. J., and J. Janssen (1989), Low temperature isotopic exchange of molecular oxygen via the reaction of NO, NH_3, and O_2 over supported vanadia and molybdena catalysts, *Catal. Lett.*, *2*, 385–394.

Blunier, T., B. Barnett, M. L. Bender, and M. B. Hendricks (2002), Biological oxygen productivity during the last 60,000 years from triple oxygen isotope measurements, *Global Biogeochem. Cycles*, *16*(3), 1029, doi:10.1029/2001GB001460.

Brasseur, G. P., and S. Solomon (2005), *Aeronomy of the Middle Atmosphere*, Springer, Dordrecht, Netherlands.

Brasseur, G. P., M. H. Hitchman, S. Walters, M. Dymek, E. Falise, and M. Pirre (1990), An interactive chemical dynamic radiative two-dimensional model of the middle atmosphere, *J. Geophys. Res.*, *95*(D5), 5639–5655, doi:10.1029/JD095iD05p05639.

Fleurat-Lessard, P., S. Y. Grebenshchikov, R. Schinke, C. Janssen, and D. Krankowsky (2003), Isotope dependence of the $O+O_2$ exchange reaction: Experiment and theory, *J. Chem. Phys.*, *119*(9), 4700–4712.

Gao, Y. Q., and R. A. Marcus (2007), An approximate theory of ozone isotope effects: Rate constant ratios and pressure dependence, *J. Chem. Phys.*, *127*, 244,316.

Guy, R. D., J. A. Berry, M. L. Fogel, and T. C. Hoering (1989), Differential fractionation of oxygen isotopes by cyanide-resistant and cyanice-sensitive respiration in plants, *Planta*, *177*, 483–491.

Guy, R. D., M. L. Fogel, and J. A. Berry (1993), Photosynthetic fractionation of the stable isotopes of oxygen and carbon, *Plant Physiol.*, *101*, 37–47.

Hathorn, B. C., and R. A. Marcus (2000), An intramolecular theory of the mass-independent isotope effect for ozone. II. Numerical implementation at low pressures using a loose transition state, *J. Chem. Phys.*, *113*(21), 9497–9509.

He, B., G. Olack, and A. Colman (2012), Pressure baseline correction and high precision CO_2 clumped-isotope (Δ_{47}) measurements in bellows and micro-volume modes, *Rapid Commun. Mass Spectrom.*, *26*(24), 2837–2853.

Holton, J. R., P. H. Haynes, M. E. McIntyre, A. R. Douglass, R. B. Rood, and L. Pfister (1995), Stratosphere-troposphere exchange, *Rev. Geophys.*, *33*(4), 403–439, doi:10.1029/95RG02097.

Holzer, M., C. Orbe, and F. W. Primeau (2012), Stratospheric mean residence time and mean age on the tropopause: Connections and implications for observational constraints, *J. Geophys. Res.*, *117*, D12314, doi:10.1029/2012JD017547.

Huntington, K. W., et al. (2009), Methods and limitations of "clumped" CO_2 isotope (Δ_{47}) analysis by gas-source isotope ratio mass spectrometry, *J. Mass Spectrom.*, *44*(9), 1318–1329.

Ianni, J. C. (2003), A comparison of the Bader-Deuflhard and the Cash-Karp Runge-Kutta integrators for the Gri-Mech 3.0 model based on the chemical kinetics code Kintecus, in *Computational Fluid and Solid Mechanics 2003*, edited by K. J. Bathe, pp. 1368–1372, Elsevier Science Ltd., Oxford, U. K.

Janssen, C. (2005), Intramolecular isotope distribution in heavy ozone, *J. Geophys. Res.*, *110*, D08308, doi:10.1029/2004JD005479.

Janssen, C., and B. Tuzson (2010), Isotope evidence for ozone formation on surfaces, *J. Phys. Chem. A*, *114*, 9709–9719.

Kaye, J. A., and D. F. Strobel (1983), Enhancement of heavy ozone in the Earth's atmosphere?, *J. Geophys. Res.*, *88*(C13), 8447–8452, doi:10.1029/JC088iC13p08447.

Kowalski, W. J., and W. P. Bahnfleth (2000), Effective UVGI system design through improved modeling, *ASHRAE Trans.*, *106*(2), 1–10.

Landais, A., V. Masson-Delmotte, N. Combourieu Nebout, J. Jouzel, T. Blunier, M. Leuenberger, D. Dahl-Jensen, and S. Johnsen (2007), Millenial scale variations of the isotopic composition of atmospheric oxygen over Marine Isotopic Stage 4, *Earth Planet. Sci. Lett.*, *258*, 101–113.

Luz, B., E. Barkan, M. L. Bender, M. H. Thiemens, and K. A. Boering (1999), Triple-isotope composition of atmospheric oxygen as a tracer of biosphere productivity, *Nature*, *400*(6744), 547–550.

Macko, P., P. Veis, and G. Cernogora (2004), Study of oxygen atom recombination on a Pyrex surface at different wall temperatures by means of time-resolved actinometry in a double pulse discharge technique, *Plasma Sources Sci. Technol.*, *13*, 251–262.

Mauersberger, K., B. Erbacher, D. Krankowsky, J. Günther, and R. Nickel (1999), Ozone isotope enrichment: Isotopomer-specific rate coefficients, *Science*, *283*, 370–372.

Modest, M. F. (2013), *Radiative Heat Transfer*, 3rd ed., 904 pp., Academic Press, New York.

Orbe, C., M. Holzer, and L. M. Polvani (2012), Flux distributions as robust diagnostics of stratosphere-troposphere exchange, *J. Geophys. Res.*, *117*, D01302, doi:10.1029/2011JD016455.

Robichaud, D. J., L. Y. Yeung, D. A. Long, M. Okumura, D. K. Havey, J. T. Hodges, C. E. Miller, and L. R. Brown (2009), Experimental line parameters of the $b\Sigma_g^+ \leftarrow X^3\Sigma_g^-$ band of oxygen isotopologues at 760 nm using frequency-stabilized cavity ring-down spectroscopy, *J. Phys. Chem. A*, *113*, 13,089–13,099.

Sander, S. P., et al. (2011), *Chemical Kinetics and Photochemical Data for Use in Atmospheric Studies: Evaluation Number 17*, JPL Publication 10–6, Jet Propul. Lab., Pasadena, Calif.

Schinke, R., S. Y. Grebenshchikov, M. V. Ivanov, and P. Fleurat-Lessard (2006), Dynamical studies of the ozone isotope effect: A status report, *Annu. Rev. Phys. Chem.*, *57*, 625–661.

Schoeberl, M. R. (2004), Extratropical stratosphere-troposphere mass exchange, *J. Geophys. Res.*, *109*, D13303, doi:10.1029/2004JD004525.

Severinghaus, J. P., R. Beaudette, M. A. Headly, K. Taylor, and E. J. Brook (2009), Oxygen-18 of O_2 records the impact of abrupt climate change on the terrestrial biosphere, *Science*, *324*(5933), 1431–1434.

Škerlak, B., M. Sprenger, and H. Wernli (2014), A global climatology of stratosphere-troposphere exchange using the ERA-Interim data set from 1979–2011, *Atmos. Chem. Phys.*, *14*, 913–937.

Starokon, E. V., M. V. Parfenov, S. E. Malykhin, and G. I. Panov (2011), Catalytic role of O^- radicals in the low-temperature isotopic exchange in dioxygen, *J. Phys. Chem. C*, *115*(25), 12,554–12,559.

Stolper, D. A., A. L. Sessions, A. A. Ferreira, E. V. S. Neto, A. Schimmelmann, S. S. Shusta, D. L. Valentine, and J. M. Eiler (2014), Combined ^{13}C-D and D-D clumping in methane: Methods and preliminary results, *Geochim. Cosmochim. Acta*, *126*, 169–191.

Tribelhorn, M. J., and M. E. Brown (1995), Thermal decomposition of barium and strontium peroxides, *Thermochim. Acta*, *255*, 143–154, doi:10.1016/0040-6031(94)02156-I.

Vinnikov, K. Y., and N. C. Grody (2003), Global warming trend of mean tropospheric temperature observed by satellites, *Science*, *302*(5643), 269–272.

Vinnikov, K. Y., N. C. Grody, A. Robock, R. J. Stouffer, P. D. Jones, and M. D. Goldberg (2006), Temperature trends at the surface and in the troposphere, *J. Geophys. Res.*, *111*, D03106, doi:10.1029/2005JD006392.

Wang, Z., E. A. Schauble, and J. M. Eiler (2004), Equilibrium thermodynamics of multiply substituted isotopologues of molecular gases, *Geochim. Cosmochim. Acta*, *68*(23), 4779–4797.

Waugh, D. W., et al. (2013), Tropospheric SF_6: Age of air from the Northern Hemisphere midlatitude surface, *J. Geophys. Res. Atmos.*, *118*, 11,429–11,441, doi:10.1002/jgrd.50848.

Wiegel, A. A., A. S. Cole, K. J. Hoag, E. L. Atlas, S. M. Schauffler, and K. A. Boering (2013), Unexpected variations in the triple oxygen isotope composition of stratospheric carbon dioxide, *Proc. Natl. Acad. Sci. U.S.A.*, *110*(44), 17,680–17,685.

Wiegell, M. R., N. W. Larsen, T. Pedersen, and H. Egsdard (1997), The temperature dependence of the exchange reaction between oxygen atoms and dioxygen molecules studied by means of isotopes and spectroscopy, *Int. J. Chem. Kinet.*, *29*(10), 745–753.

Yang, H., and K. K. Tung (1996), Cross-isentropic stratosphere-troposphere exchange of mass and water vapor, *J. Geophys. Res.*, *101*(D5), 9413–9423, doi:10.1029/96JD00057.

Yeung, L. Y., E. D. Young, and E. A. Schauble (2012), Measurements of $^{18}O^{18}O$ and $^{17}O^{18}O$ in the atmosphere and the role of isotope-exchange reactions, *J. Geophys. Res.*, *117*, D18306, doi:10.1029/2012JD017992.

Yoshino, K., J. R. Esmond, A. S.-C. Cheung, D. E. Freeman, and W. H. Parkinson (1992), High resolution absorption cross sections in the transmission window region of the Schumann-Runge bands and Herzberg continuum of O_2, *Planet. Space Sci.*, *40*(2/3), 185–192.

Young, E. D., L. Y. Yeung, and I. E. Kohl (2014), On the $\Delta^{17}O$ budget of atmospheric O_2, *Geochim. Cosmochim. Acta*, *135*, 102–125.